



Brain MR image classification for Alzheimer's disease diagnosis using structural hippocampal asymmetrical attributes from directional 3-D log-Gabor filter responses

Katia M. Poloni^a, Italo A. Duarte de Oliveira^a, Roger Tam^b, Ricardo J. Ferrari^{a,*}, for the Alzheimer's Disease Neuroimaging Initiative¹

^a Department of Computing, Federal University of São Carlos, Rod. Washington Luis, Km 235, 13565-905 São Carlos, SP, Brazil

^b Department of Radiology, School of Biomedical Engineering, University of British Columbia, Djavad Mowafaghian Centre for Brain Health, 2215 Wesbrook Mall, V6T 2B5 Vancouver, Canada

ARTICLE INFO

Article history:

Received 19 February 2020

Revised 28 May 2020

Accepted 27 July 2020

Available online 1 September 2020

Communicated by Cuntai Guan

Keywords:

Structural hippocampal asymmetries

3D log-Gabor filters

Alzheimer's disease

Magnetic resonance imaging

MR image classification

ABSTRACT

Alzheimer's disease (AD) is a progressive and irreversible neurodegenerative condition whose development is characterized by lateralized brain atrophies. In AD, the hippocampus is the first brain structure to present atrophy, which, although to a lesser extent, is also a precursor to the broader asymmetrical development of the human brain. Structural magnetic resonance (MR) imaging is capable of detecting the disease-induced anatomical changes in the brain, thus aiding the diagnosis of AD. MR image attributes extracted from the hippocampal regions are commonly used for the AD classification task. However, most of the published methods do not explore hippocampal asymmetries for image classification. In this study, we propose a new technique for performing the classification of MR images for AD using only hippocampal asymmetrical attributes. By using the new proposed asymmetry index (*AI*), we assessed the attributes and the ones that passed the analysis of variance test, i.e., showing statistically mean differences among the classes (CN, MCI, and AD), were selected for classification. As a result of our study, the statistical analysis of our *AI* has shown a significant increase in hippocampal asymmetry as disease progress (CN < MCI < AD). Moreover, for the classification using clinical MR images, we obtained accuracy values of 69.44% and 82.59%; and AUC values of 0.76 and 0.9 for CN × MCI and CN × AD, respectively. Last, we found the results of our asymmetry analysis consistent with other statistical assessments and our classification results, using only asymmetry attributes comparable to (or even higher than) existing hippocampus studies.

© 2020 Published by Elsevier B.V.

1. Introduction

Alzheimer's disease (AD) is a progressive and irreversible neurodegenerative disease predominantly affecting the elderly and corresponding up to 80% of all dementia cases [1]. As advancing age is the most significant risk factor for developing AD, with the

increase in life expectancy, this disease has become one of the most significant health problems in the world [2,1]. Histologically, AD is associated with an excessive accumulation of amyloid- β protein on extracellular plaques and deposition of hyperphosphorylated tau protein in intracellular neurofibrillary tangles [3], which can lead to the death of the neurons.

The human brain exhibits a high level of structural hemispherical symmetry that decreases with aging [4,5], and it is even more acutely affected by the presence of pathological conditions [6], which is the case of AD. The structural hemispherical asymmetry progression in AD is often characterized by regional gray matter loss with the degradation process affecting first and more severely, the left-hemisphere regions [7]. In Alzheimer's, several studies have been exploring the degree of brain symmetry loss in magnetic resonance (MR) images, especially of the hippocampal regions, as a

* Corresponding author.

E-mail address: rferarri@ufscar.br (R.J. Ferrari).

URL: <https://biggroup.dc.ufscar.br> (R.J. Ferrari).

¹ Data used in preparation of this article were obtained from the Alzheimer's Disease Neuroimaging Initiative (ADNI) database (adni.loni.usc.edu). As such, the investigators within the ADNI contributed to the design and implementation of ADNI and/or provided data but did not participate in analysis or writing of this report. A complete listing of ADNI investigators can be found at: http://adni.loni.usc.edu/wp-content/uploads/how_to_apply/ADNI_Acknowledgement_List.pdf.

way to develop biomarkers for AD [8,9]. Shi et al. [10] have conducted a meta-analysis of MRI studies to assess volume reduction and asymmetry patterns in MCI and AD and found lower values of bilateral hippocampal volume loss and atrophy in MCI when compared to AD and a consistent left-less-than-right asymmetry pattern in all groups, but with different extents. Furthermore, computer vision and artificial intelligence techniques that perform the analysis using the whole-brain or hippocampal regions, and incorporate anatomical knowledge, such as anatomical landmarks and subfield atlases, have been developed to facilitate decision making [6].

The hippocampus is a brain structure located in the medial temporal lobe with a decisive role in the formation and retention of episodic memory [8]. In the presence of cognitive disease, it is one of the first brain structures to endure atrophy, besides being the precursor to the broader asymmetrical development of the human brain [11,12].

Structural magnetic resonance imaging (MRI) has been playing an increasingly significant role in clinical trials and studies related to Alzheimer's. The main reason is its high sensitivity in detecting subtle structural brain changes [13], which results in images with superior contrast and exquisite anatomical details. This property makes it possible to detect disease-induced anatomical changes in the brain [14] and help with the AD diagnosis.

Over the past years, several studies have assessed hemispheric asymmetries in MR images, mostly focusing on healthy populations stratified by sex [15–17,4,18] and handedness [16,19]. Moreover, some studies have evaluated brain asymmetry under the influence of cognitive disease, i.e., autism and developmental language disorder [20], epilepsy [21], AD [9,8,22,23], and Parkinson's disease on DaTSCAN images [24]. Among these studies, the ones assessing asymmetries in AD usually have concentrated on the differences in the left and right hippocampus and reported an increasing asymmetry ratio with aging that grows with AD development [9,8,22]. However, except for the work of Barnes and his colleagues [22], that adopts manual segmentation, they rely on the proper automatic segmentation of the hippocampus to quantify the asymmetrical differences. Furthermore, these studies did not have a goal of image classification using asymmetrical features, but only in studying asymmetry on the different conditions of AD.

Martins et al. [21] have proposed a framework to model normal structural brain asymmetry from control subjects, but they have not considered the AD classification using their model. There are many studies in the literature that extract and use MR [25–30] and single-photon emission computed tomography (SPECT) [31–35] image attributes for automatic the classification of CN, MCI, and AD. More recently, deep neural networks have been used with the same purpose [36,37], however, despite the high accuracy shown by these methods, they also present high complexity, which implies in a large number of hyperparameters to be estimated and the need for a large number of images for training the models. Moreover, these models are difficult to interpret, considering the imaging anatomy provided for training them [38].

In this study, we propose a new technique to perform MR image classification for AD using only attributes presenting significant differences among our diagnosis groups (CN, MCI, and AD) when tested for asymmetry using the one-way analysis of variance (ANOVA) test. As statistical attributes, we use the first four moments (mean, variance, skewness, and kurtosis) computed from the magnitude maps of directional log-Gabor filter responses of hippocampal regions in MR images. The attributes that passed the ANOVA test were used to train Support Vector Machine (SVM) models to classify clinical MR images in $CN \times MCI$ and $CN \times AD$.

Although the performance of our proposed method is not as high as the performance of some works proposed in the literature,

we are convinced that our method can be used as a complementary approach as it explores an important element not evaluated by other classification methods, which is the hippocampal asymmetry analysis on AD development. Besides, our method explores well-established anatomical changes signaling the progression of Alzheimer's disease, which is the ones affecting the hippocampal regions, and, therefore, it is easy to explain and interpret the results. Moreover, the low dimensionality of the devised feature vectors has great benefits for classifier design, since a relatively small sample size is required for this task, especially compared to the deep learning methods and considering the limited number of images samples typically available for neuroimaging studies.

The structure of the rest of this paper is organized as follows. Section 2 and 3 provide, respectively, a description of the image datasets and all methods and processes used in this research. Section 4 presents the experimental results of our statistical analysis and image classification using the asymmetrical attributes. Finally, Section 5 concludes the paper and briefly outlines future work.

2. Datasets

In this study, we used MR images from both the Neuroimage Analysis Center (NAC) [39] and the Alzheimer's Disease Neuroimaging Initiative (ADNI) [40].

The NAC dataset consists of 149 3-D triangular meshes, each representing a distinct brain structure. The meshes are spatially aligned to a T1-weighted (T1-w) and T2-weighted (T2-w) MRI sequences of a healthy, 42-year-old male patient. The images were acquired using a Siemens 3T scanner with an isotropic voxel size of 0.75 mm. This dataset also contains a downsampled version of both acquisitions at 1 mm isotropic resolution with a matrix size of $256 \times 256 \times 256$ voxels. For this study, we only used the T1-w image with 1 mm isotropic resolution and the two hippocampal 3-D triangular meshes.

The ADNI image dataset contains images acquired using a wide variety of 1.5T and 3T MRI scanners and protocols from the three leading manufacturers (Philips, General Electric, and Siemens), and over 50 sites across the USA and Canada². Consequently, the image specifications (e.g., size, resolution) are diverse and will be omitted here. In this study, the ADNI images were limited to images acquired using only the MPRAGE sequence³, and for patients with age between 70–85 years, among the three diagnostic groups, i.e., CN, MCI, and mild-AD, and with the MMSE data provided. With these restrictions, a total of 762 unique images (one image for each subject) were randomly selected. The images cohort demographics are shown in Table 1.

For the image preprocessing detailed in Section 3.1, we used the NAC T1-w image as a reference, and for the classification tasks, we used the ADNI T1-w MRI study images.

3. Methods

As illustrated in Fig. 1, our method starts by first preprocessing all ADNI MR brain images. Then, for each image, we extract the two hemispheres and flip the left one so they can have approximately the same spatial location. After that, in the directional filtering step, we perform a convolution of the image hemispheres with a bank of 3-D log-Gabor filters and save all directional responses. Next, by constraining the region of interest (ROI) to the hippocampal region using a binary template mask, we compute the first four statistical moments (mean, variance, skewness, and kurtosis) of the

² <http://adni.loni.usc.edu/about/centers-cores/study-sites/>.

³ These MPRAGE files are considered the best in the quality ratings and have undergone preprocessing steps - <http://adni.loni.usc.edu/methods/mri-tool/mri-analysis/>.

Table 1
Cohort demographics of the dataset used in this study.

	CN	MCI	AD
No. of subjects	302	251	209
Age ($\mu \pm \sigma$; range)	75.79 \pm 4.14 (70–85)	76.80 \pm 4.30 (70–85)	77.12 \pm 4.43 (70–85)
MMSE ($\mu \pm \sigma$; range)	29.56 \pm 0.50 (29–30)	27.04 \pm 0.82 (26–28)	22.15 \pm 2.76 (4–25)
Gender (F:M)	151:151	80:171	94:115

MMSE stands for Mini-Mental State Examination.

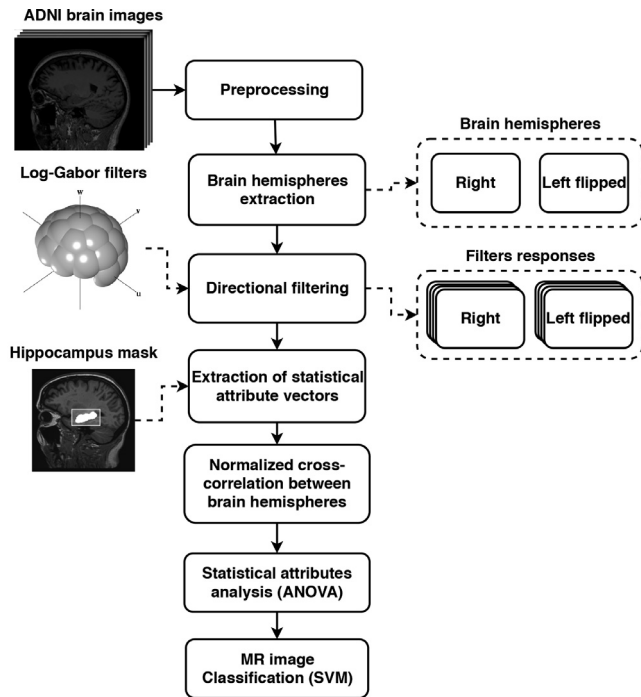


Fig. 1. Overview of the proposed method.

filtered hemisphere images to characterize the intensity distribution inside the ROI. For each brain hemisphere, we save the values of each computed moment in a vector. Later, we compute the normalized cross-correlation between the corresponding left and right vectors of each statistical moment and check the asymmetry index (AI) among the diagnosis groups using ANOVA. Finally, we use all the moments showing significant statistical differences among the classes to train SVM classifiers for the image classification task.

3.1. Preprocessing

In this study, we first processed all MR images for noise reduction using the Non-Local Means technique [41], followed by bias field correction with the N4-ITK technique [42] and image intensity standardization using the histogram matching algorithm proposed in [43], with the T1-w template image from the NAC dataset [39] used as a reference image. We then aligned the study (ADNI) images to the NAC T1-w template image using spatial affine transformations provided by the Nifty-Reg image registration tool [44]. Next, we performed brain extraction on all images using the ROBEX [45] technique. Finally, to properly delimit the hippocampal regions, we conducted a deformable image registration [46] between the NAC T1-w template and all study images. Different from the first image registration, we used each study image as a reference to get the transformation, which we then applied to the provided hippocampal mesh models for defining the regions of interest.

3.2. Brain hemispheres extraction

The precise identification of the symmetry plane is a crucial task for a correct evaluation of hemisphere-wise asymmetries [6]. In this study, we first detected the midsagittal plane (MSP) in the brain MR images using the phase congruency technique proposed by Ferrari et al. [47]. Then, we translated the brain for its gravity center and rotated it to keep the MSP parallel to the sagittal coordinates. Finally, we flipped the left hemisphere to keep both hemispheres at approximately the same spatial location.

3.3. Directional filtering

In this study, we conducted image filtering in the frequency domain using a bank of 3-D log-Gabor filters designed in the Fourier domain following the mathematical formulation proposed by Dosil et al. [48]. Besides having zero DC components and, therefore, not responding to regions with constant intensities, the log-Gabor filters have extended tails covering high frequencies, which allows getting a wide bandwidth that can provide uniform coverage of the frequency domain.

3.3.1. Log-Gabor filters

Each 3-D log-Gabor filter is defined by the multiplication of a radial and an angular term as

$$G(\boldsymbol{\rho}; \omega_s, \eta_\beta, \theta_i, \phi_{ij}) = \underbrace{\exp\left(-\frac{\log^2(\|\boldsymbol{\rho}\|/\omega_s)}{2\log^2\eta_\beta}\right)}_{\text{radial}} + \underbrace{\exp\left(-\frac{\alpha(\boldsymbol{\rho}, \theta_i, \phi_{ij})}{2\sigma_z^2}\right)}_{\text{angular}}, \quad (1)$$

where $\alpha(\boldsymbol{\rho}, \theta_i, \phi_{ij}) = \arccos^2\left(\frac{\mathbf{v} \cdot \boldsymbol{\rho}}{\|\boldsymbol{\rho}\|}\right)$, $\boldsymbol{\rho} = (u, v, w)$ is a point in the Fourier domain, and $\mathbf{v} = (\cos \theta_i \cos \phi_{ij}, \cos \theta_i \sin \phi_{ij}, \sin \theta_i)$ contains the spherical coordinate system angles, with θ_i and ϕ_{ij} being the elevation and azimuth angles of the filter, respectively. Additionally, the filter frequency coverage can be modified by changing the parameters ω_s , which is the central frequency for scale $s = \{0, 1, \dots, N_s - 1\}$, and $\eta_\beta = \sigma_\omega/\omega_s$ and σ_z , which controls the frequency bandwidth and angular spread of the filter, respectively.

Parameters description and values. The central frequency ω_s is computed as $\omega_s = \omega_{\max}/\gamma^s$, where γ is a scaling factor (in the radial direction) between successive filters in the bank. The elevation angle is computed as

$$\theta_i = \frac{\pi i}{2(N_e - 1)}, \quad (2)$$

where $i = \{0, 1, \dots, N_e - 1\}$ and N_e correspond respectively to the indices and the number of elevation angles. In our implementation of the 3-D log-Gabor filter bank, the elevation is uniformly sampled, while azimuth varies as a function of elevation to keep the density of filters constant. This is achieved by keeping an equal arc-length between adjacent azimuth values over the unit radius sphere instead of taking uniform angular distances [48]. Therefore, the number of filters varies with the elevations as

$$N_a(i) = N_{a,0} \cos \theta_i, \quad (3)$$

where $N_{a,0}$ is the number of azimuth angles in the equator of a unit-radius sphere. Once the number of azimuth filters per elevation is obtained, a central azimuth angle ϕ_{ij} , for the i th elevation, can be computed as

$$\phi_{ij} = \begin{cases} \frac{\pi j}{N_{a,0}}, & \text{if } i = 0 \\ \frac{2\pi j}{N_a(i)}, & \text{otherwise} \end{cases}, \quad (4)$$

where $j = \{0, 1, \dots, N_a(i) - 1\}$.

In our study, the shape of the 3D log-Gabor filters was visually defined with the help of a Matlab tool, designed (and kindly provided to our group) by Dosil et al. [48], as illustrated in Fig. 2. The main goal of our filter bank design was to create isotropic filters since we are not interested in filtering any particular orientation of the hippocampal structures in the MR image. The parameter values that best achieved the uniform spectral coverage using isotropic filters with minimum overlap were the following: scaling factor ($\gamma = 1.2$), filter bandwidth ($\eta_\beta = 0.55$), and angular deviation ($\sigma_\alpha = 1.2$).

To define the number of scales (N_s), azimuth angles ($N_{a,0}$), elevation angles (N_e), and maximum central frequency (ω_{\max}), we conducted an exploratory experiment using 40 MR images (20 CN and 20 AD) not included in the test group. For that, we performed an analysis using all combinations of the following parameter values $N_s = 2, 3$, and 4, $N_{a,0} = 4, 6$, and 8, $N_e = 3, 4$, and 5 and $\omega_{\max} = 0.25, 0.30, 0.35$, and 0.4. In addition, similar to the work of Padilla et al. [31], we used the Fisher discriminant function [49], computed for each statistical measure (mean, variance, skewness, and kurtosis), as the figure of merit to be maximized. The best results were obtained for the variance measure with the following combination of parameters ($N_s = 3, N_{a,0} = 6, N_e = 4$ and $\omega_{\max} = 0.25$, or 0.3), so we refined our search for the ω_{\max} in the [0.25–0.30] interval, with a step of 0.01. As a result, we found $\omega_{\max} = 0.28$ as the best parameter value. Such parameters resulted in 23 filter orientations per scale, represented here as $\Theta_s = (\theta_i, \phi_{ij})$. Fig. 2 shows a visual representation of the bank of log-Gabor filters constructed with these parameters.

3.3.2. Filters responses

The filtering process was performed using the brain hemispheres encephalon (right and left flipped) to avoid artifacts on the resultant filtered image that can be caused by the abrupt boundary truncation. The hippocampal binary mask was further used to restrict the region of interest for the analysis.

For each orientation, we computed the directional resulting image by taking the largest pixel-wise magnitude response, $A_{\Theta_s}(\mathbf{x})$, across all scales, defined as

$$DR_{\Theta}(\mathbf{x}) = \max_{0 \leq s < N_s} (A_{\Theta_s}(\mathbf{x})), \quad (5)$$

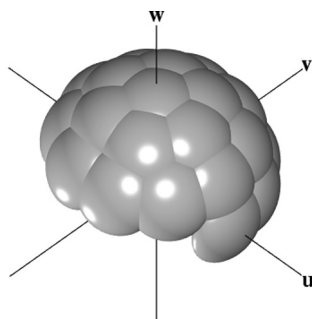


Fig. 2. Illustration of the bank of 3-D log-Gabor filters used in this work.

where $\mathbf{x} = (i, j, k)$ denotes a spatial location in the image domain.

Second-order moment. Having the summarized directional responses, denoted as $DR_{\Theta}(\mathbf{x})$, we also calculated a map of 3-D moments of order $p + q + r$ according to the formula

$$M_{p,q,r}(\mathbf{x}) = \sum_{\Theta} x_{\Theta}^p(\mathbf{x}) y_{\Theta}^q(\mathbf{x}) z_{\Theta}^r(\mathbf{x}), \quad (6)$$

where

$$x_{\Theta}(\mathbf{x}) = DR_{\Theta}(\mathbf{x}) \cos \theta_i \cos \phi_{ij}, \quad (7)$$

$$y_{\Theta}(\mathbf{x}) = DR_{\Theta}(\mathbf{x}) \cos \theta_i \sin \phi_{ij},$$

$$z_{\Theta}(\mathbf{x}) = DR_{\Theta}(\mathbf{x}) \sin \theta_i.$$

From 6, we can write a 3×3 matrix of second-order moments of inertia can be written as

$$M_{DR_{\Theta}}(\mathbf{x}) = \begin{bmatrix} M_{2,0,0}(\mathbf{x}) & M_{1,1,0}(\mathbf{x}) & M_{1,0,1}(\mathbf{x}) \\ M_{1,1,0}(\mathbf{x}) & M_{0,2,0}(\mathbf{x}) & M_{0,1,1}(\mathbf{x}) \\ M_{1,0,1}(\mathbf{x}) & M_{0,1,1}(\mathbf{x}) & M_{0,0,2}(\mathbf{x}) \end{bmatrix}, \quad (8)$$

which gives a notion of the covariance of the DR_{Θ} moments in the variables $x_{\Theta}(\mathbf{x})$, $y_{\Theta}(\mathbf{x})$ and $z_{\Theta}(\mathbf{x})$. The principal moments of inertia can be closely approximated by the eigenvalues of the $M_{DR_{\Theta}}(\mathbf{x})$ matrix (which are denoted by $\lambda_0(\mathbf{x}) \geq \lambda_1(\mathbf{x}) \geq \lambda_2(\mathbf{x}) \geq 0$) and provide a sense of local direction (at position \mathbf{x}) along which the data has the largest variance.

For devising the asymmetric attributes for the image classification, we use both the summarized directional filter responses DR_{Θ} , where $\Theta = \{0, 1, \dots, 22\}$, and the eigenvalue maps $\lambda_0(\mathbf{x})$, $\lambda_1(\mathbf{x})$, and $\lambda_2(\mathbf{x})$. Fig. 3 shows the sagittal view of the brain as a visual representation of the directional filtering step. The four values of Θ illustrated in the image correspond to the first azimuth angle combined with each one of the four elevations (e.g., $\Theta_0 = (\phi_0, \theta_0)$, ..., $\Theta_{22} = (\phi_0, \theta_3)$).

3.4. Hippocampal asymmetry analysis

The first step of our directional hippocampal asymmetry analysis is a finer modification of the binary mask used to delimit the left and right hippocampal regions. Then, we compute statistics for the pixel intensities inside the mask for both regions and compare them via normalized cross-correlation.

3.4.1. Hippocampal regions

We combined the right and left hippocampal masks to account for spatial variations of the regions and to ensure encompassing all hippocampal structures in our asymmetry analysis. For that, we applied the union operator, in a voxel-wise manner, to the masks and expanded the resulting mask with a morphological dilation operation, using a 3-D sphere of 2 voxels radius as the structuring element.

3.4.2. Extraction of statistical attributes

After the directional filter stage, we obtained 26 images (23 DR_{Θ} + the eigenvalue maps λ_0, λ_1 , and λ_2), as illustrated in Fig. 3. Then, the first four statistical moments (mean, variance, skewness, and kurtosis) were computed from the voxel intensities inside the hippocampal mask, resulting in four attribute vectors (of size $N = 26$, each) per hemisphere.

3.4.3. Normalized cross-correlation between attribute vectors of brain hemispheres

To measure how similar the attributes extracted from each brain hemisphere are, we perform the normalized cross-correlation between the corresponding left (\mathbf{a}_L) and right (\mathbf{a}_R) attribute vectors, both of size $N = 26$. For that, we first have equally zero-padded the right vector on both sides by $\frac{N}{2}$ units, resulting

in a new vector \mathbf{a}_{R^*} of size $2 \times N$. Next, the left attribute vector was slid over the right one, performing an element-wise multiplication with the part of the input currently on, summing up the results, and normalizing the values into a single output pixel. This operation is represented by

$$NCC(x) = \frac{\sum_{i=0}^{N-1} \mathbf{a}_L[i] \cdot \mathbf{a}_{R^*}[i+x]}{\sqrt{\sum_{i=0}^{N-1} \mathbf{a}_L[i]^2} \sqrt{\sum_{i=0}^{N-1} \mathbf{a}_{R^*}[i+x]^2}}, \quad (9)$$

where $x = 0, 1, \dots, N - 1$.

Note that this operation helps to identify the nature of the association between the two hemispheres and how they correlated with each other. By using such an approach, we intend not just to compare each directional response alone but to assess the overall pattern of asymmetry that each subject might have.

3.5. Statistical attributes analysis

Following the pipeline of our proposed method in Fig. 1, we first tested whether our attributes have asymmetry within the three diagnosis groups (CN, MCI, and AD), and then checked if we can classify CN \times AD and CN \times MCI based uniquely on the asymmetrical attributes devised from the study images.

3.5.1. Statistical analysis

In our statistical analysis, we propose a new hippocampal asymmetry index (AI) defined as

$$AI = 1 - \frac{1}{N} \sum_{i=0}^{N-1} NCC(x), \quad (10)$$

with AI ranging from 0 to 1, being 0 when the attribute vectors are identical (symmetry case) and 1 when there is a complete lack of correlation between the attribute vectors (asymmetric case).

One-way ANOVA test was used to test the statistically significant differences between the AI scores of our statistical attributes for the diagnosis groups (CN, MCI, and AD). For that, we inspected all AI residuals for normality and variance homogeneity. Here, all four attributes passed on the normality test but failed the variance homogeneity, except for the variance attribute. Therefore, to mitigate this problem, we applied the Yeo-Johnson power transformation [50], defined as

$$\psi(\lambda_b, AI) = \begin{cases} \frac{(AI+1)^{\lambda_b} - 1}{\lambda_b}, & \text{if } \lambda_b \neq 0, AI \geq 0 \\ \log(AI + 1), & \text{if } \lambda_b = 0, AI \geq 0 \\ -\frac{[-(-AI+1)^{2-\lambda_b} - 1]}{(2-\lambda_b)}, & \text{if } \lambda_b \neq 2, AI < 0 \\ -\log(-AI + 1), & \text{if } \lambda_b = 2, AI < 0 \end{cases}, \quad (11)$$

where λ_b is the value that maximizes the log-likelihood function.

The ANOVA test allows us to test the null hypothesis (all means are equal) against the alternative hypothesis (at least one mean differs) with a specified value of $\alpha = 0.05$. However, when using ANOVA to test the equality of at least three groups means, the results do not identify which particular differences between pairs of means are significant. Therefore, to examine the significant pairwise mean differences between groups, we use the post hoc test Tukey's honestly significant difference (HSD) [51], with $\alpha_t = 0.05$.

3.6. Image classification

For the image classification in CN \times MCI and CN \times AD diagnosis groups, we used the asymmetrical attributes, computed for each statistical measure, and which passed the ANOVA test to train SVM classifiers with different kernel types (linear, polynomial, and radial basis function (RBF)). We conducted the classification using the attributes individually and with all combinations of horizontal concatenations. Also, since we have a slightly unbalanced

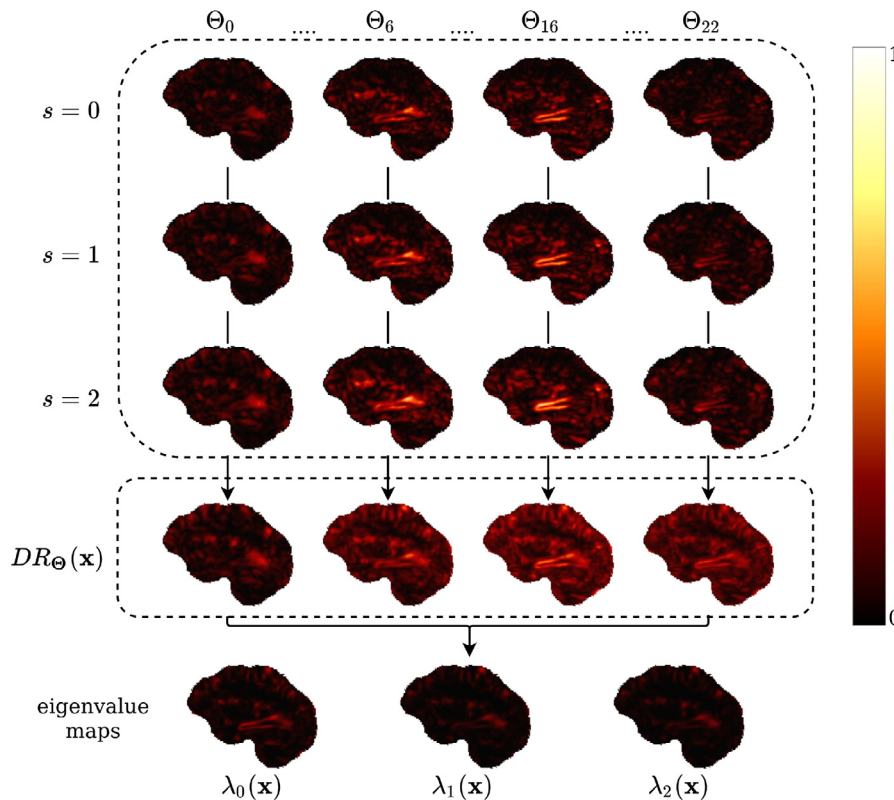


Fig. 3. Visual representation of the filters responses for the sagittal brain view.

dataset, we have automatically adjusted the model weights to be inversely proportional to class frequencies in the input data using the *class_weight*⁴ parameter from the scikit-learn python library.

We determined the hyper-parameters of the SVMs using a grid search and considering the area under the receiver operating characteristic (ROC) curve (AUC) as a performance criterion for the CN × MCI and CN × AD classification, where the AUC values were estimated in 10-fold nested cross-validation [52]. We finally calculated the classification results using accuracy (ACC), balanced accuracy (BACC), F1-score (F1), and the AUC metrics. A detailed description of these metrics can be found in [53].

4. Experimental results and discussions

In the statistical analysis, we used the four *AI* values corresponding to the normalized cross-correlation function ($NCC(x)$) of each statistical measure. We illustrated the results for the comparison of the diagnosis groups and presented the p-values of the ANOVA and post hoc tests. In the classification, we conducted seven classification experiments for CN × MCI and CN × AD with all combinations (vector concatenations) of the statistical attributes that survived to the ANOVA test.

4.1. Statistical analysis

We tested the significant differences of our *AI* statistical measures for diagnosis groups and sex differences.

4.1.1. *AI* vs. diagnosis groups

We summarize the ANOVA results for each statistical measure in the diagnosis groups in Table 2, which includes the mean and standard deviation of *AI* values, the ANOVA p-values, and the conclusions after running the Tukey's HSD post hoc test. From these analyses, we noticed the skewness has a p-value larger than 0.05, which means this statistical measure showed no significant difference between means among the diagnosis groups. According to Turkey's HSD comparison, the pairwise diagnosis groups CN × MCI and CN × AD presented statistically significant differences in all cases, but the skewness. For the MCI × AD case, the ANOVA test showed statistically significant differences only for the variance measure. Considering our post-roc conclusions, the variance measure presented a noticeable trend of asymmetry, that is, the *AI* variance values are lower in CN than MCI, and MCI than AD. This trend, which has been reported in other papers in the neurology literature [9,8], shows an increase in brain hemispheres asymmetry as Alzheimer's severity increases. Furthermore, the conclusions for the mean and kurtosis measures, despite not having reported results for the MCI × AD pairwise comparison, have also reported this trend for the other two pairwise comparisons, with lower *AI* values in CN than MCI and CN than AD. Fig. 4(a) shows the boxplot of the variance measure for the population stratified by diagnosis groups. In this case, it can be appreciated that the *AI* values increase as Alzheimer's severity increases.

4.1.2. *AI* vs. sex

Table 3 presents the mean and standard deviation of *AI* values for sex analysis. The p-values by sex have present statistically significant difference in all cases (p-value < 0.05), except for the skewness (p-value > 0.05). In addition, we can notice that *AI* values are slightly lower for the female group for measures passing the ANOVA test. Fig. 4(b) shows the boxplot of the variance measure for the population stratified by sex.

4.2. Classification

In our statistical analysis of the attribute measures, the skewness has shown no statistically significant mean differences between groups and, therefore, since our purpose was to show the predictive power of asymmetry attributes, we performed our classification experiments using only the statistical measures that survived at ANOVA, i.e., the mean, variance, and kurtosis measures. In addition, we conducted classification only between CN × MCI and CN × AD classes since the variance was the only measure showing significant mean difference between the MCI × AD classes.

Although in our classification experiments we tested different SVM kernel functions, the best results were obtained using the polynomial kernel with degree = 1 and, therefore, we present and discuss the classification results only for this kernel. The best parameter *C* (in terms of maximizing the AUC value) of each SVM classifier was determined in a coarse-grid search with a range of values [2^{-5} ; 2^{10}] and steps defined by a base of 2 with the exponent incremented by 0.5, i.e., 2^{-5} , $2^{-4.5}$, ..., 2^{10} ; followed by a finer search in the neighborhood of the best coarse-grid parameter, \tilde{C} , with a grid range of values [$2^{(\log_2 \tilde{C})-2}$; $2^{(\log_2 \tilde{C})+2}$] and steps defined by a base of 2 with the exponent incremented by 0.25.

For classification using individually the three measures that passed to the statistical symmetry analysis, we have the highest classification result for the variance in both experiments CN × MCI and CN × AD classifications, with AUC values of 0.74 and 0.88, respectively. Table 4 presents the average classification results of the 10-fold nested cross-validation for all three measures.

After the classification experiments using individual attributes, we tested all combinations (vector concatenations) of the attribute vectors. Table 5 shows the average classification results for the 10-fold nested cross-validation of this new experiment. For visual simplicity, we have abbreviated the names of the statistical attributes by concatenating parts of them, e.g., Mean&Var&Kurt, meaning concatenations of the mean, variance, and kurtosis attribute vectors. Analyzing the results in Table 5, we can notice that attribute vectors concatenation has a positive influence on the AUC results. Particularly, the concatenations involving the variance attribute have provided higher gains. The improvement also happens when all measures are considered together, resulting in AUC values of 0.76 and 0.90 for the CN × MCI and CN × AD classifications, respectively.

Fig. 5(a) and (b) show the ROC curves and their corresponding AUC values for the CN × MCI and CN × AD classification, respectively. These ROC curves referred to the results in Table 5. From these curves, we can notice that although our accuracy values are lower than some of the results reported in the literature, we obtained high AUC values. This can be explained by considering that the experiments were performed using a slightly unbalanced dataset, and unlike accuracy, the AUC is insensitive to this class ill-balance [54]. Overall, the results from our proposed approach are very encouraging if we take into account the classification experiments used only asymmetric hippocampal attributes.

4.3. Comparison with a common ROI-based method

Different from other methods that develop indices and metrics based on the volumes of the hippocampus and its respective sub-fields for statistical analysis of asymmetries in CN, MCI, and AD subjects [9,8], our method aims to classify MR images using asymmetrical features extracted from the hippocampal regions, without the requirement of image segmentation and volume assessment. However, we have not found other methods in the literature

⁴ <http://scikit-learn.org/stable/modules/generated/sklearn.svm.SVC.html>

Table 2
Mean and standard deviation of AI values by diagnosis group and results of ANOVA ($\alpha = 0.05$) and post hoc comparisons survived at Tukey HSD ($\alpha_t < 0.05$).

Asymmetry Index	CN	MCI	AD	ANOVA <i>p</i> -value	post hoc
Mean	0.6332 ± 0.0099	0.6389 ± 0.0073	0.6382 ± 0.0075	< 0.001	CN < MCI, CN < AD
Variance	0.7120 ± 0.0083	0.7162 ± 0.0088	0.7182 ± 0.0095	< 0.001	CN < MCI, MCI < AD, CN < AD
Kurtosis	0.6776 ± 0.0716	0.7099 ± 0.0803	0.7165 ± 0.0869	< 0.001	CN < MCI, CN < AD
Skewness	0.3198 ± 0.0313	0.3235 ± 0.0321	0.3209 ± 0.0315	0.399	Not significant

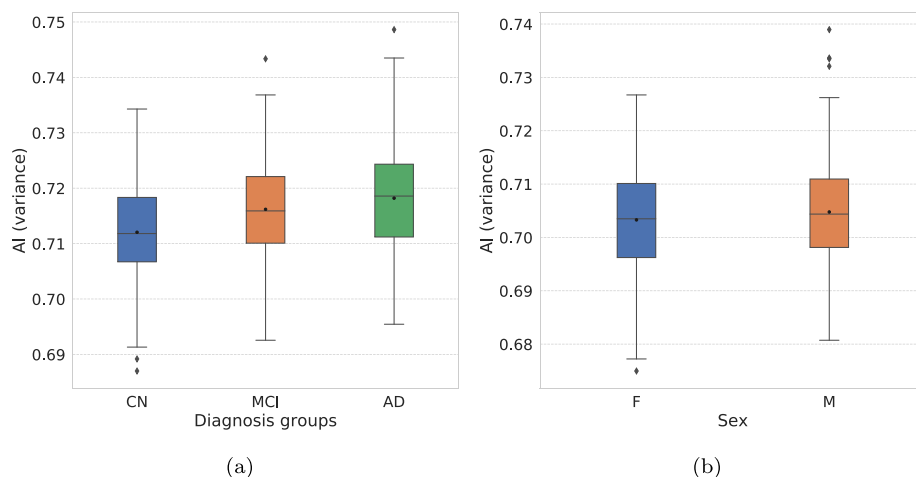


Fig. 4. Boxplots of AI mean differences of the variance measure by (a) diagnosis groups and (b) gender.

Table 3
Mean and standard deviation of AI values by sex along with the results of ANOVA ($\alpha = 0.05$).

Asymmetry Index	F	M	ANOVA <i>p</i> -value
Mean	0.6209 ± 0.0105	0.6236 ± 0.0079	< 0.001
Variance	0.7033 ± 0.0093	0.7048 ± 0.0096	0.033
Kurtosis	0.6707 ± 0.0763	0.6997 ± 0.0870	< 0.001
Skewness	0.2962 ± 0.0331	0.2945 ± 0.0326	0.497

performing classification of MR images in Alzheimer's disease using only asymmetric features.

For comparison, we have implemented a region of interest (ROI) based method, which is frequently used as a baseline in many published papers in the literature [55,2,36,56,57], and applied it to the same image dataset used in this study to assess the relative performance of our asymmetrical attributes. To this end, we have extracted ROI-specific features from the MR images using the GM normalized volume of ninety ROIs (forty-five for each hemisphere) as features for the SVM classification. Specifically, the brain images are segmented into three different tissue types (i.e., gray matter (GM), white matter (WM), and cerebrospinal fluid (CSF)), using the FAST technique [58] implemented in the FSL package.⁵ Then, using a deformable registration algorithm [46] included in the Nifty Reg software,⁶ we aligned all ninety pre-defined ROIs in the cerebrum, provided by the anatomical automatic labeling (AAL) atlas [59], to each subject of our database. The AAL map is originally defined on the Montreal Neurological Institute (MNI) single subject brain MR image [60]. Next, we computed the volumes of the GM, WM, and CSF tissues inside each of those ninety ROIs. Finally, the GM volumes were normalized by the total intracranial volume and used as a feature representation of each MR image. The total

intracranial volume was estimated by the summation of GM, WM, and CSF volumes from all ROIs.

For a fair comparison, we have performed a grid-search on the SVM hyperparameters to achieve the best results for this method, since the number of subjects is different from the aforementioned papers using this method. In this case, we have trained the SVM models using 10-fold nested cross-validation and performed the hyper-parameters search for the same kernels and parameter intervals used in our experiments.

The best result obtained for the CN × AD using the ROI-based method was 0.91 ± 0.04 of AUC, with 81.61% ± 6.48% of ACC, 80.72% ± 6.84% of BACC, and 0.77 ± 0.08 of F1-score. This result was achieved with the SVM classifier using a polynomial kernel of degree one. For the CN × MCI experiment, the best result was 0.8 ± 0.05 of AUC, with 72.68% ± 4.08% of ACC, 72.82% ± 3.78% of BACC, and 0.71 ± 0.04 of F1-score, and it was obtained using the SVM classifier with an RBF kernel.

Comparing the above results with the ones from our method in Table 5, we observed that our method has comparable classification results for the CN × AD case, but its performance is still lower than the baseline method for the CN × MCI case. Despite the results, our method uses only information extracted for the hippocampi regions, while the ROI-based method uses image information from ninety ROIs, and it heavily relies on the success of the image segmentation method being used.

5. Conclusions and future work

In this paper, we propose a new technique to perform the classification of MR images for AD using only structural hippocampal asymmetrical attributes from directional responses of 3-D log-Gabor filters. For that, we developed a new asymmetry index and used it to test each proposed statistical attribute to verify whether they could be meaningful to assess hippocampal asymmetries and, therefore, to aid the diagnosis of AD.

⁵ <http://fsl.fmrib.ox.ac.uk/fsl/fslwiki>.

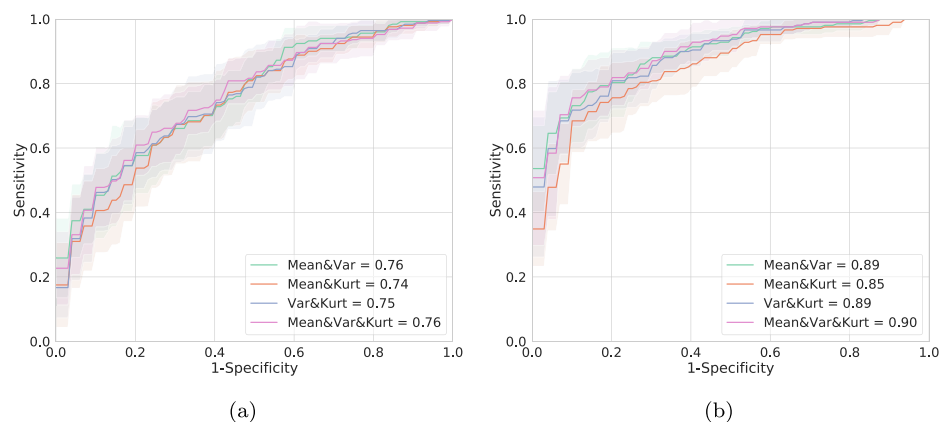
⁶ <http://cmictig.cs.ucl.ac.uk/wiki/index.php/NiftyReg>

Table 4Average \pm std classification results of the nested 10-fold cross-validation for each statistical measure.

Statistics	CN \times MCI				CN \times AD			
	AUC	ACC(%)	BACC(%)	F1 – score(%)	AUC	ACC(%)	BACC(%)	F1 – score(%)
Mean	0.71 \pm 0.05	67.44 \pm 6.01	67.76 \pm 6.25	0.66 \pm 0.08	0.82 \pm 0.03	73.77 \pm 4.58	73.83 \pm 4.51	0.70 \pm 0.05
Variance	0.74 \pm 0.04	68.18 \pm 4.65	68.36 \pm 4.84	0.67 \pm 0.06	0.88 \pm 0.03	80.42 \pm 5.43	80.63 \pm 5.24	0.77 \pm 0.06
Kurtosis	0.70 \pm 0.08	65.47 \pm 6.06	64.52 \pm 6.08	0.59 \pm 0.08	0.79 \pm 0.07	76.33 \pm 6.48	75.33 \pm 6.96	0.70 \pm 0.09

Table 5Average \pm std classification results of the nested 10-fold cross-validation for the combinations of the statistical measures.

Statistics	CN \times MCI				CN \times AD			
	AUC	ACC(%)	BACC(%)	F1 – score(%)	AUC	ACC(%)	BACC(%)	F1 – score(%)
Mean&Var	0.76 \pm 0.05	65.65 \pm 4.47	65.64 \pm 4.48	0.63 \pm 0.05	0.89 \pm 0.04	80.42 \pm 5.43	80.35 \pm 5.16	0.77 \pm 0.06
Mean&Kurt	0.74 \pm 0.07	68.53 \pm 5.57	68.36 \pm 5.99	0.65 \pm 0.08	0.85 \pm 0.04	78.09 \pm 5.12	77.59 \pm 5.30	0.74 \pm 0.06
Var&Kurt	0.75 \pm 0.06	66.53 \pm 6.43	66.39 \pm 6.32	0.64 \pm 0.07	0.89 \pm 0.04	81.04 \pm 6.80	80.74 \pm 6.56	0.77 \pm 0.07
Mean&Var&Kurt	0.76 \pm 0.06	69.44 \pm 4.58	69.31 \pm 4.85	0.66 \pm 0.07	0.90 \pm 0.04	82.59 \pm 6.49	81.36 \pm 6.64	0.78 \pm 0.08

**Fig. 5.** ROC curves and corresponding AUC values for the (a) CN \times MCI and (b) CN \times AD classification results, respectively.

Most methods proposed in the literature exploring hippocampal asymmetries in MR images for AD [9,8] use the volume of sub-field structures, thus depending on the success of image segmentation techniques, and focus on the development of biomarkers for the AD progression, not exploring the asymmetrical attributes for the AD classification. Instead, our method extracts asymmetric attributes via image filtering and uses them for image classification.

Our technique achieved accuracies of 69.44% and 82.59%, and AUCs of 0.76 and 0.90, respectively, for the CN \times MCI and CN \times AD classification. Although these results are not as high as some other reported results (e.g., accuracy values around 80% for CN \times MCI and 90% for CN \times AD), we would like to emphasize that in this study we have only used structural hippocampal asymmetrical attributes for the MR image classification and the number of subjects used to assess our method was larger than most of the published works. Besides, we believe our method could be used as a complementary approach to other methods that do not take into account hippocampal asymmetry in their analysis.

Despite the encouraging results, further investigation should be conducted to explore new attributes to characterize hippocampal asymmetries. Special attention will be given to find attributes capable of classifying MR images between MCI and AD groups.

6. Funding Statement

The authors would like to thank the Fundação de Amparo à Pesquisa do Estado de São Paulo (FAPESP) (processes 2018/08826–9, 2018/06049–5, and 2018/09972–9), the Coordenação de

Aperfeiçoamento de Pessoal de Nível Superior (CAPES) – Finance Code 001, and Conselho Nacional de Desenvolvimento Científico e Tecnológico (CNPq) for the financial support of this research.

Credit authorship contribution statement

Katia M. Poloni: Conceptualization, Methodology, Software, Writing – original draft. **Italo A. Duarte de Oliveira:** Methodology, Software, Writing – original draft. **Roger Tam:** Writing – review & editing. **Ricardo J. Ferrari:** Supervision, Writing – review & editing.

Declaration of Competing Interest

The authors declare that they have no known competing financial interests or personal relationships that could have appeared to influence the work reported in this paper.

Acknowledgments

Data collection and sharing for this project was funded by the Alzheimer’s Disease Neuroimaging Initiative (ADNI) (National Institutes of Health Grant U01 AG024904) and DOD ADNI (Department of Defense award number W81-XWH-12-2-0012). ADNI is funded by the National Institute on Aging, the National Institute of Biomedical Imaging and Bioengineering, and through generous contributions from the following: AbbVie, Alzheimer’s Association; Alzheimer’s Drug Discovery Foundation; Araclon Biotech; BioClinica, Inc.; Biogen; Bristol-Myers Squibb Company; CereSpir,

Inc.; Cogstate; Eisai Inc.; Elan Pharmaceuticals, Inc.; Eli Lilly and Company; EuroImmun; F. Hoffmann-La Roche Ltd and its affiliated company Genentech, Inc.; Fujirebio; GE Healthcare; IXICO Ltd.; Janssen Alzheimer Immunotherapy Research & Development, LLC.; Johnson & Johnson Pharmaceutical Research & Development LLC.; Lumosity; Lundbeck; Merck & Co., Inc.; Meso Scale Diagnostics, LLC.; NeuroRx Research; Neurotrack Technologies; Novartis Pharmaceuticals Corporation; Pfizer Inc.; Piramal Imaging; Servier; Takeda Pharmaceutical Company; and Transition Therapeutics. The Canadian Institutes of Health Research is providing funds to support ADNI clinical sites in Canada. Private sector contributions are facilitated by the Foundation for the National Institutes of Health (www.fnih.org). The grantee organization is the Northern California Institute for Research and Education, and the study is coordinated by the Alzheimer's Therapeutic Research Institute at the University of Southern California. ADNI data are disseminated by the Laboratory for Neuro Imaging at the University of Southern California.

References

- [1] Alzheimer's Association, Alzheimer's disease facts and figures, *Alzheimer's & Dementia: The Journal of the Alzheimer's Association* 15 (3) (2019) 321–387.
- [2] J. Zhang, M. Liu, L. An, Y. Gao, D. Shen, Alzheimer's disease diagnosis using landmark-based features from longitudinal structural MR images, *IEEE Journal of Biomedical and Health Informatics* 21 (5) (2017) 1607–1616.
- [3] H.S. Bassiony, M.B. Zickri, H.G. Metwally, H.A. Elsharif, S.M. Alghandour, W. Sakr, Comparative histological study on the therapeutic effect of green tea and stem cells in Alzheimer's disease complicating experimentally induced diabetes, *International Journal of Stem Cells* 8 (2) (2015) 181–190.
- [4] R.M. Lucarelli, R.T. P., R. McColl, K. Hulsey, C. Ayers, A.R. Whittemore, K.S. King, MR imaging of hippocampal asymmetry at 3T in a multiethnic, population-based sample: results from the Dallas Heart Study, *American Journal of Neuroradiology* 34 (4) (2013) 752–757.
- [5] X. Long, L. Zhang, W. Liao, C. Jiang, B. Qiu, Alzheimer's Disease Neuroimaging Initiative, Distinct laterality alterations distinguish mild cognitive impairment and Alzheimer's disease from healthy aging: statistical parametric mapping with high resolution MRI, *Human Brain Mapping* 34 (12) (2013) 3400–3410.
- [6] S.X. Liu, Symmetry and asymmetry analysis and its implications to computer-aided diagnosis: A review of the literature, *Journal of Biomedical Informatics* 42 (6) (2009) 1056–1064.
- [7] A.W. Toga, P.M. Thompson, Mapping brain asymmetry, *Nature Reviews Neuroscience* 4 (1) (2003) 37–48.
- [8] B.A. Ardekani, S.A. Hadid, E. Blessing, A.H. Bachman, Sexual dimorphism and hemispheric asymmetry of hippocampal volumetric integrity in normal aging and Alzheimer disease, *American Journal of Neuroradiology* 40 (2) (2019) 276–282.
- [9] A. Sarica, R. Vasta, F. Novellino, M.G. Vaccaro, A. Cerasa, A. Quattrone, A.D.N. Initiative, et al., MRI asymmetry index of hippocampal subfields increases through the continuum from the Mild Cognitive Impairment to the Alzheimer's disease, *Frontiers in Neuroscience* 12 (576) (2018) 1–12.
- [10] F. Shi, B. Liu, Y. Zhou, C. Yu, T. Jiang, Hippocampal volume and asymmetry in mild cognitive impairment and Alzheimer's disease: Meta-analyses of MRI studies, *Hippocampus* 19 (11) (2009) 1055–1064.
- [11] A.A. Woolard, S. Heckers, Anatomical and functional correlates of human hippocampal volume asymmetry, *Psychiatry Research: Neuroimaging* 201 (1) (2012) 48–53.
- [12] T. Guadalupe, M.P. Zwiers, A. Teumer, K. Wittfeld, A.A. Vasquez, M. Hoogman, P. Hagoort, G. Fernandez, J. Buitelaar, K. Hegenscheid, et al., Measurement and genetics of human subcortical and hippocampal asymmetries in large datasets, *Human Brain Mapping* 35 (7) (2014) 3277–3289.
- [13] K.A. Johnson, N.C. Fox, R.A. Sperling, W.E. Klunk, Brain imaging in Alzheimer disease, *Cold Spring Harbor Perspectives in Medicine* 2 (4) (2012) a006213-1–23.
- [14] Y. Luo, X. Tang, Automated diagnosis of Alzheimer's disease with multi-atlas based whole brain segmentations, in: *Medical Imaging 2017: Biomedical Applications in Molecular, Structural, and Functional Imaging*, SPIE, Bellingham, Washington, 2017, pp. 275–283.
- [15] J. Ashburner, C. Hutton, R. Frackowiak, I. Johnsrude, C. Price, K. Friston, Identifying global anatomical differences: Deformation-based morphometry, *Human Brain Mapping* 6 (5–6) (1998) 348–357.
- [16] C.D. Good, I. Johnsrude, J. Ashburner, R.N. Henson, K.J. Friston, R.S. Frackowiak, Cerebral asymmetry and the effects of sex and handedness on brain structure: a voxel-based morphometric analysis of 465 normal adult human brains, *Neuroimage* 14 (3) (2001) 685–700.
- [17] E. Luders, C. Gaser, L. Jancke, G. Schlaug, A voxel-based approach to gray matter asymmetries, *Neuroimage* 22 (2) (2004) 656–664.
- [18] V.A. Kovalev, F. Kruggel, D.Y. von Cramon, Structural brain asymmetry as revealed by 3D texture analysis of anatomical MR images, in: *Object Recognition Supported by User Interaction for Service Robots*, IEEE, Quebec, Canada, 2002, pp. 808–811.
- [19] P.Y. Hervé, F. Crivello, G. Percey, B. Mazoyer, N. Tzourio-Mazoyer, Handedness and cerebral anatomical asymmetries in young adult males, *Neuroimage* 29 (4) (2006) 1066–1079.
- [20] M.R. Herbert, D.A. Ziegler, C.K. Deutsch, L.M. O'Brien, D.N. Kennedy, P.A. Filipek, A.I. Bakardjiev, J. Hodgson, M. Takeoka, N. Makris, et al., Brain asymmetries in autism and developmental language disorder: a nested whole-brain analysis, *Brain* 128 (1) (2005) 213–226.
- [21] S.B. Martins, B.C. Benato, B.F. Silva, C.L. Yasuda, A.X. Falcão, Modeling normal brain asymmetry in MR images applied to anomaly detection without segmentation and data annotation, *Medical Imaging 2019: Computer-Aided Diagnosis*, vol. 10950, SPIE, San Diego, California, 2019, p. 109500C.
- [22] J. Barnes, R.I. Schill, J.M. Schott, C. Frost, M.N. Rossor, N.C. Fox, Does Alzheimer's disease affect hippocampal asymmetry? Evidence from a cross-sectional and longitudinal volumetric MRI study, *Dementia and Geriatric Cognitive Disorders* 19 (5–6) (2005) 338–344.
- [23] P.M. Thompson, K.M. Hayashi, G. De Zubicaray, A.L. Janke, S.E. Rose, J. Semple, D. Herman, M.S. Hong, S.S. Dittmer, D.M. Doodrell, et al., Dynamics of gray matter loss in Alzheimer's disease, *Journal of Neuroscience* 23 (3) (2003) 994–1005.
- [24] A. Ortiz, J. Munilla, M. Martínez, J.M. Gorriç, J. Ramírez, D. Salas-Gonzalez, Parkinson's disease detection using isosurfaces-based features and Convolutional Neural Networks, *Frontiers in Neuroinformatics* 13 (48) (2019) 48.
- [25] L. Sørensen, C. Igel, N. Liv Hansen, M. Osler, M. Lauritzen, E. Rostrup, M. Nielsen, Early detection of Alzheimer's disease using MRI hippocampal texture, *Human Brain Mapping* 37 (3) (2016) 1148–1161.
- [26] P. Coupé, S.F. Eskildsen, J.V. Manjón, V.S. Fonov, D.L. Collins, Alzheimer's disease Neuroimaging Initiative, et al., Simultaneous segmentation and grading of anatomical structures for patient's classification: application to Alzheimer's disease, *NeuroImage* 59 (4) (2012) 3736–3747.
- [27] P. Coupé, S.F. Eskildsen, J.V. Manjón, V.S. Fonov, J.C. Pruessner, M. Allard, D.L. Collins, Alzheimer's Disease Neuroimaging Initiative, et al., Scoring by nonlocal image patch estimator for early detection of Alzheimer's disease, *NeuroImage: Clinical* 1 (1) (2012) 141–152.
- [28] O.B. Ahmed, M. Mizotin, J. Benois-Pineau, M. Allard, G. Catheline, C.B. Amar, Alzheimer's Disease Neuroimaging Initiative, et al., Alzheimer's disease diagnosis on structural MR images using circular harmonic functions descriptors on hippocampus and posterior cingulate cortex, *Computerized Medical Imaging and Graphics* 44 (2015) 13–25.
- [29] O.B. Ahmed, J. Benois-Pineau, M. Allard, C.B. Amar, G. Catheline, Alzheimer's Disease Neuroimaging Initiative, et al., Classification of Alzheimer's disease subjects from MRI using hippocampal visual features, *Multimedia Tools and Applications* 74 (4) (2015) 1249–1266.
- [30] F.J. Martínez-Murcia, J.M. Górriz, J. Ramírez, A. Ortiz, Alzheimer's Disease Neuroimaging Initiative, et al., A spherical brain mapping of MR images for the detection of Alzheimer's disease, *Current Alzheimer Research* 13 (5) (2016) 575–588.
- [31] P. Padilla, J.M. Górriz, J. Ramírez, R. Chaves, F. Segovia, I. Álvarez, D. Salas-González, M. López, C.G. Puntonet, Alzheimer's disease detection in functional images using 2D Gabor wavelet analysis, *Electronics Letters* 46 (8) (2010) 556–558.
- [32] J. Stoessel, G. Fung, SVM feature selection for classification of SPECT images of Alzheimer's disease using spatial information, in: *Fifth IEEE International Conference on Data Mining (ICDM'05)*, IEEE, Houston, Texas, 2005, pp. 8–pp.
- [33] I. Álvarez, M. López, J.M. Górriz, J. Ramírez, D. Salas-Gonzalez, C.G. Puntonet, F. Segovia, Automatic classification system for the diagnosis of Alzheimer disease using component-based SVM aggregations, in: *Advances in Neuro-Information Processing*, Springer, Berlin, Heidelberg, 2008, pp. 402–409.
- [34] J. Ramírez, J.M. Górriz, M. López, D. Salas-Gonzalez, I. Álvarez, F. Segovia, C.G. Puntonet, Early detection of the Alzheimer disease combining feature selection and kernel machines, in: *Advances in Neuro-Information Processing*, Springer, Berlin, Heidelberg, 2008, pp. 410–417.
- [35] D. Salas-Gonzalez, J.M. Górriz, J. Ramírez, M. López, I. Álvarez, F. Segovia, C.G. Puntonet, Computer aided diagnosis of Alzheimer disease using support vector machines and classification trees, in: *Advances in Neuro-Information Processing*, Springer, Berlin, Heidelberg, 2008, pp. 418–425.
- [36] M. Liu, J. Zhang, E. Adeli, D. Shen, Landmark-based deep multi-instance learning for brain disease diagnosis, *Medical Image Analysis* 43 (1) (2018) 157–168.
- [37] K. Aderghal, J. Benois-Pineau, K. Afdel, C. Gwenaëlle, Fuseme: Classification of sMRI images by fusion of deep CNNs in 2D+ ϵ projections, in: *International Workshop on Content-Based Multimedia Indexing*, ACM, Florence, Italy, 2017, pp. 1–7.
- [38] T. Jo, K. Nho, A.J. Saykin, Deep learning in Alzheimer's disease: diagnostic classification and prognostic prediction using neuroimaging data, *Frontiers in Aging Neuroscience* 11 (2019) 220.
- [39] M. Halle, I. Talos, M. Jakab, N. Makris, D. Meier, L. Wald, B. Fischl, R. Kikinis, Multi-modality MRI-based atlas of the brain, <http://www.spl.harvard.edu/publications/item/view/2037> (2017).
- [40] C.R.J. Jack, M.A. Bernstein, N.C. Fox, G. Thompson, P. Alexander, D. Harvey, B. Borowski, P.J. Britton, J.L. Whitwell, C. Ward, A.M. Dale, J.P. Felmlee, J.L. Gunter, D.L. Hill, R. Killiany, N. Schuff, S. Fox-Bosetti, C. Lin, C. Studholme, C.S. DeCarli, G. Krueger, H.A. Ward, G.J. Metzger, K.T. Scott, R. Mallozzi, D. Blezek, J. Levy, J.P. Debbins, A.S. Fleisher, M. Albert, R. Green, G. Bartzokis, G. Glover, J. Mugler, M.

- W. Weiner, The Alzheimer's disease neuroimaging initiative (ADNI): MRI methods, *Journal of Magnetic Resonance Imaging* 27 (4) (2017) 685–691.
- [41] A. Buades, B. Coll, J.-M. Morel, A review of image denoising algorithms, with a new one, *Multiscale Modeling & Simulation* 4 (2) (2005) 490–530.
- [42] N.J. Tustison, B.B. Avants, P.A. Cook, Y. Zheng, A. Egan, P.A. Yushkevich, J.C. Gee, N4ITK: improved N3 bias correction, *IEEE Transactions on Medical Imaging* 29 (6) (2010) 1310–1320.
- [43] L.G. Nyúl, J.K. Udupa, X. Zhang, New variants of a method of MRI scale standardization, *IEEE Transactions on Medical Imaging* 19 (2) (2000) 143–150.
- [44] S. Ourselin, R. Stefanescu, X. Pennec, Robust registration of multi-modal images: Towards real-time clinical applications, in: *Medical Image Computing and Computer-Assisted Intervention – MICCAI*, Springer, Heidelberg, Berlin, 2002, pp. 140–147.
- [45] J.E. Iglesias, C.-Y. Liu, P.M. Thompson, Z. Tu, Robust brain extraction across datasets and comparison with publicly available methods, *IEEE Transactions on Medical Imaging* 30 (9) (2011) 1617–1634.
- [46] M. Modat, G.R. Ridgway, Z.A. Taylor, M. Lehmann, J. Barnes, D.J. Hawkes, N.C. Fox, S. Ourselin, Fast free-form deformation using graphics processing units, *Computer Methods and Programs in Biomedicine* 98 (3) (2010) 278–284.
- [47] R.J. Ferrari, C.H. Villa-Pinto, C.A.F. Moreira, Detection of the midsagittal plane in MR images using a sheetness measure from eigenanalysis of local 3D phase congruency responses, in: *International Conference on Image Processing (ICIP)*, IEEE, Phoenix, Arizona, 2016, pp. 2335–2339.
- [48] R. Dostil, X.M. Pardo, X.R. Fdez-Vidal, Decomposition of three-dimensional medical images into visual patterns, *IEEE Transactions on Biomedical Engineering* 52 (12) (2005) 2115–2118.
- [49] A.J. Izenman, *Linear discriminant analysis*, in: *Modern Multivariate Statistical Techniques*, Springer, New York, NY, 2013, pp. 237–280.
- [50] I.-K. Yeo, R.A. Johnson, A new family of power transformations to improve normality or symmetry, *Biometrika* 87 (4) (2000) 954–959.
- [51] H. Abdi, L.J. Williams, Tukey's honestly significant difference (hsd) test, *Encyclopedia of Research Design* 3 (1) (2010) 1–5.
- [52] M.J. Abdulaal, A.J. Casson, P. Gaydecki, Performance of nested vs. non-nested SVM cross-validation methods in visual BCI: Validation study, in: *European Signal Processing Conference (EUSIPCO)*, IEEE, Rome, Italy, 2018, pp. 1680–1684.
- [53] J.D. Kelleher, B. Mac Namee, A. D'arcy, *Fundamentals of machine learning for predictive data analytics: algorithms, worked examples, and case studies*, first ed., MIT Press, Cambridge, Massachusetts, 2015.
- [54] A. Narasimhamurthy, An overview of machine learning in medical image analysis: Trends in health informatics, in: *Medical Imaging: Concepts, Methodologies, Tools, and Applications*, IGI Global, Hershey, Pennsylvania, 2017, pp. 36–58.
- [55] J. Zhang, Y. Gao, Y. Gao, B.C. Munsell, D. Shen, Detecting anatomical landmarks for fast Alzheimer's disease diagnosis, *IEEE Transactions on Medical Imaging* 35 (12).
- [56] M. Liu, C. Lian, D. Shen, Anatomical-landmark-based deep learning for Alzheimer's disease diagnosis with structural magnetic resonance imaging, in: *Intelligent Systems Reference Library*, Springer, Cham, 2020, pp. 127–147.
- [57] M. Liu, J. Zhang, E. Adeli, D. Shen, Deep multi-task multi-channel learning for joint classification and regression of brain status, in: *International Conference on Medical Image Computing and Computer-Assisted Intervention – MICCAI*, Cham, 2017, pp. 3–11.
- [58] Y. Zhang, M. Brady, S. Smith, Segmentation of brain MR images through a hidden Markov random field model and the expectation-maximization algorithm, *IEEE Transactions on Medical Imaging* 20 (1) (2001) 45–57.
- [59] N. Tzourio-Mazoyer, B. Landeau, D. Papathanassiou, F. Crivello, O. Etard, N. Delcroix, B. Mazoyer, M. Joliot, Automated anatomical labeling of activations in SPM using a macroscopic anatomical parcellation of the MNI MRI single-subject brain, *Neuroimage* 15 (1) (2002) 273–289.
- [60] D.L. Collins, A.P. Zijdenbos, V. Kollokian, J.G. Sled, N.J. Kabani, C.J. Holmes, A.C. Evans, Design and construction of a realistic digital brain phantom, *IEEE Transactions on Medical Imaging* 17 (3) (1998) 463–468.



Italo Antonio Duarte de Oliveira is currently enrolled in a Bachelor degree in Computer Engineering at the Federal University of São Carlos, Brazil. His current research interests include digital image processing and machine learning.



Roger Tam obtained his Ph.D. in computer science in 2004 from the University of British Columbia (UBC) in the research area of computational geometry, shape modelling, and visualization. He has been a faculty member in the Department of Radiology at UBC since 2007, and a founding member of the UBC School of Biomedical Engineering since 2018. His research interests center on image analysis, machine learning, and precision medicine.



Ricardo José Ferrari is an Associate professor in the Department of Computing (DC) at the Federal University of São Carlos (UFSCar). He holds BSc. (Dec/1995), MSc (Mar/1998) and Ph.D. (Mar/2002) degrees in Electrical Engineering from the University of São Paulo (USP – São Carlos) with specialization in Medical Image Processing. In the period from Feb/1999 to Feb/2000, he worked on the experimental part of his Ph.D. thesis at the University of Calgary, Canada. Dr. Ferrari has also conducted two postdoctoral degrees: the first one at the Seaman Family MR Research Center (Calgary-Canada, 2003) and the second at Sunnybrook Hospital (Toronto-Canada, 2007). Previously to join the UFSCar, he worked as a research engineer for several years in Canada. His researches are in the areas of multidimensional signal processing, statistical modeling, machine learning, computer vision, and pattern recognition. Applications include systems to aid early diagnosis of degenerative brain diseases and dynamic analysis of cells in intravital microscopy images.



Katia Maria Poloni received her MSc in Computer Science in 2018 from the Federal University of São Carlos (UFSCar), Brazil, and her BSc degree in Computer Science in 2016 from the State University of Londrina (UEL), Brazil. Since 2018, she has been a Ph.D. student at the UFSCar. Her research is mainly related to the automatic detection of structural brain changes in MR images of Alzheimer patients.